Ttc30a affects tubulin modifications in a model for ciliary chondrodysplasia with polycystic kidney disease

Maike Getwan[a,b,c], Anselm Hoppmann[d], Pascal Schlosser[d], Kelli Grand[a,b,c], Weiting Song[c], Rebecca Diehl[c], Sophie Schroda[c], Florian Heeg[c], Konstantin Deutsch[e], Friedhelm Hildebrandt[e], Ekkehart Lausch[f], Anna Köttgen[d], and Soeren S. Lienkamp[a,b,c,1]

[a]Institute of Anatomy, University of Zurich, 8057 Zurich, Switzerland; [b]Swiss National Centre of Competence in Research Kidney Control of Homeostasis, University of Zurich, 8057 Zurich, Switzerland; [c]Renal Division, Department of Medicine, Faculty of Medicine, Medical Center – University of Freiburg, 79110 Freiburg, Germany; [d]Institute of Genetic Epidemiology, Faculty of Medicine, Medical Center – University of Freiburg, 79110 Freiburg, Germany; [e]Department of Pediatrics, Boston Children's Hospital, Harvard Medical School, Boston, MA 02115; and [f]Department of Pediatrics, Faculty of Medicine, Medical Center – University of Freiburg, 79110 Freiburg, Germany

Edited by Richard M. Harland, University of California, Berkeley, CA, and approved August 4, 2021 (received for review April 12, 2021)

Skeletal ciliopathies (e.g., Jeune syndrome, short rib polydactyly syndrome, and Sensenbrenner syndrome) are frequently associated with nephronophthisis-like cystic kidney disease and other organ manifestations. Despite recent progress in genetic mapping of causative loci, a common molecular mechanism of cartilage defects and cystic kidneys has remained elusive. Targeting two ciliary chondrodysplasia loci (*ift80* and *ift172*) by CRISPR/Cas9 mutagenesis, we established models for skeletal ciliopathies in *Xenopus tropicalis*. Froglets exhibited severe limb deformities, polydactyly, and cystic kidneys, closely matching the phenotype of affected patients. A data mining–based in silico screen found *ttc30a* to be related to known skeletal ciliopathy genes. CRISPR/Cas9 targeting replicated limb malformations and renal cysts identical to the models of established disease genes. Loss of Ttc30a impaired embryonic renal excretion and ciliogenesis because of altered posttranslational tubulin acetylation, glycylation, and defective axoneme compartmentalization. *Ttc30a/b* transcripts are enriched in chondrocytes and osteocytes of single-cell RNA-sequenced embryonic mouse limbs. We identify TTC30A/B as an essential node in the network of ciliary chondrodysplasia and nephronophthisis-like disease proteins and suggest that tubulin modifications and cilia segmentation contribute to skeletal and renal ciliopathy manifestations of ciliopathies in a cell type–specific manner. These findings have implications for potential therapeutic strategies.

cilia | chondrodysplasia | cystic kidney disease | tubulin modifications | *Xenopus*

Primary cilia are hair-like appendages that extend from the surface of most differentiated cells. Their functional impairment or loss results in ciliopathies (1, 2). Ciliopathies can affect a range of organ systems and tissues, including the kidneys, liver, eyes, testes, brain, and skeleton. Often, multiple organ manifestations occur in combination (e.g., Bardet–Biedl Syndrome affecting kidney, brain, eyes, gonads, and digit number), but depending on the affected locus, only certain combinations of phenotypes may co-occur (3, 4).

Most genes affected by mutations in ciliopathy patients encode for structural components of the primary cilium (1–3). Some protein groups colocalize to ciliary subcompartments and are associated with common clinical features. Examples are the Bardet–Biedl-related BBSome components at the base of cilia (5), proteins in the proximal cilium that are mainly linked to nephronophthisis (6), or components of the axonemal intraflagellar transport (IFT) machinery linked to skeletal ciliopathies (SC) such as Jeune's asphyxiating thoracic dysplasia (JATD), Mainzer-Saldino syndrome (MZSDS), Sensenbrenner syndrome, or Cranioectodermal dysplasia (4, 7, 8). However, many ciliopathy proteins don't adhere to these categories. For example, mutations of basal body genes (*CEP120*) were identified in SC patients (4, 9), and IFT components (*IFT27* and *IFT74*) can cause Bardet–Biedl syndrome (10, 11). Thus, the molecular cause of the variability and clinical overlap of certain ciliopathy manifestations is elusive.

Despite recent advances in genetics that identified most genes affected in ciliopathies and studies of the ciliary proteome in cell culture models, the understanding of ciliary protein compositions and their function in each specific tissue remains incomplete (12–14). Posttranslational modifications (PTMs) of axonemal tubulin by polyglycylation and glutamylation contribute to the "tubulin code" that diversifies tubulin function and supports the structural integrity of cilia (15–17). In vitro studies have shown that ciliary polyglutamylation by TTLL5 and TTLL6 depends on the Joubert syndrome–associated proteins ARL13B and CEP41 (18, 19), but if tubulin PTMs are defective in other ciliopathies or contribute to the phenotypic pleiotropy remains unknown.

One subgroup of ciliopathies affects patients with skeletal deformities (4, 9). Typical phenotypes of SCs are shortened ribs resulting in a narrow thorax, truncated limbs (micromelia), shortened fingers (brachydactyly), and multiple digits (polydactyly). In some cases, the kidneys (nephronophthisis or cystic kidneys), eyes (retinopathy), liver function (liver fibrosis, liver cysts), or left–right axis formation (situs inversus) can be affected.

The Hedgehog (Hh) signaling pathway is one of many cellular signals that is frequently found to be disrupted by defective

Significance

Cilia are tubulin-based cellular appendages, and their dysfunction has been linked to a variety of genetic diseases. Ciliary chondrodysplasia is one such condition that can co-occur with cystic kidney disease and other organ manifestations. We modeled skeletal ciliopathies by mutating two established disease genes in *Xenopus tropicalis* frogs. Bioinformatic analysis identified *ttc30a* as a ciliopathy network component, and targeting it replicated skeletal malformations and renal cysts as seen in patients and the amphibian models. A loss of Ttc30a affected cilia by altering posttranslational tubulin modifications. Our findings identify TTC30A/B as a component of ciliary segmentation essential for cartilage differentiation and renal tubulogenesis. These findings may lead to novel therapeutic targets in treating ciliary skeletopathies and cystic kidney disease.

Author contributions: M.G. and S.S.L. designed research; M.G., A.H., P.S., K.G., W.S., R.D., S.S., F. Heeg, K.D., F. Hildebrandt, E.L., and A.K. performed research; M.G., A.H., P.S., K.G., A.K., and S.S.L. analyzed data; and M.G. and S.S.L. wrote the paper.

The authors declare no competing interest.

This article is a PNAS Direct Submission.

[1]To whom correspondence may be addressed. Email: soeren.lienkamp@uzh.ch.

This article contains supporting information online at https://www.pnas.org/lookup/suppl/doi:10.1073/pnas.2106770118/-/DCSupplemental.

Published September 21, 2021.

ciliary function (20–32). The ciliary Hh pathway is required for chondrocyte proliferation, differentiation, and limb patterning (33–36). Two of the best-characterized SC genes are *ift80* (37–39) (mutated in SRPS III and IV and JATD) and *ift172* (40–42) (mutated in JATD and MZSDS). Both encode IFT-B subcomplex proteins (43), and although genetic interactions were described, they do not interact physically with each other (40, 43, 44). In model organisms, biallelic loss-of-function mutations result in shortened, missing, or fewer cilia. Morphant and mutant zebrafish larvae have pronephric glomerular cysts, retinal degeneration, pericardial edema, slightly smaller eyes, and a curved tail (39, 40, 45). In addition, *ift172* morphants have otolith defects, hydrocephalus, and craniofacial cartilage defects (40). In mice, null alleles of *ift80* or *ift172* are prenatally lethal (20, 24), while mice with hypomorphic alleles have a low survival rate and suffer from shortening of long bones, a narrow thorax, and polydactyly (24, 46, 47). Chondrocyte-specific loss of function of either gene in conditional knockout mice results in severely shortened limbs (48, 49). Conditional Col2α1; IFT80$^{fl/fl}$ mice revealed that chondrocytes are disorganized, the growth plate is smaller, and articular cartilage is thickened (48, 50). Loss of *ift80* or *ift172* reduces the expression of Hedgehog target genes, such as *patched1* or *gli1* (24, 47), in line with the hypothesis that Ift80 acts downstream of Smoothened as its agonist SAG, and the second messenger Gli2 can rescue the loss of *Ift80* (48). Embryonic renal dysplasia has been observed in mice with hypomorphic alleles of *ift172*, but no studies have addressed their role in kidney function.

Mutations in at least 27 known disease genes currently account for most genetic diagnoses in cases of SC (4). However, because SC is a rare genetic disorder, the known causal genes might not cover the complete spectrum of genes relevant to the pathophysiology of SC. A more complete understanding of the molecular network of SC proteins is needed to shed light on its pathogenesis and offer potential therapeutic options.

Here, we describe two models for chondrodysplasia using CRISPR/Cas9–mediated editing of *ift80* and *ift172* in *Xenopus*. CRISPR-targeted froglets developed severe limb defects during metamorphosis with shortened limbs due to chondrocyte differentiation defects, syn- and polydactyly, and polycystic kidneys, phenocopying major clinical features of ciliary chondrodysplasia. Impaired ciliogenesis was detected in multiciliated cells (MCCs) and resulted in defective fluid excretion during tadpole stages. Using a data-mining approach, we identified candidate genes with similar molecular properties to the established disease genes. Among these, only *ttc30a* targeting mimicked the full spectrum of chondrodysplasia phenotypes (i.e., impaired ciliogenesis, fluid retention in tadpoles, polycystic kidneys, and strongly affected limb development, including polydactyly in froglets). Thus, Ttc30a acts in ciliary signaling disrupted in chondrodysplasia and cystic kidney disease. Enhanced expression in chondrocytes and osteocytes of Ttc30a1 and Ttc30b suggest an evolutionarily conserved role in mammals. Together, our findings identify TTC30A/B as a critical node in the pathogenesis network of ciliary chondrodysplasia with polycystic kidney disease.

Results

CRISPR/Cas9 Targeting of *ift80* and *ift172* Leads to Chondrodysplasia and Cystic Kidneys in *Xenopus tropicalis*. We chose *Xenopus* to establish a model for ciliary chondrodysplasia because it is an aquatic organism that allows for analysis of limb development, has a high sequence conservation to humans, is an established model in cilia research, and provides good experimental access (50–54). We targeted two well characterized SC genes (*ift80* and *ift172*) for loss-of-function analysis using CRISPR/Cas9–based genome editing. Indel frequency and knockout scores were used to identify highly effective single guide RNAs (sgRNAs) against both targets in *X. tropicalis* embryos (*SI Appendix*, Fig. 1 *A*–*C*). Injection of F0 embryos with Cas9/sgRNA ribonucleoprotein (RNP) resulted in mosaic gene disruption and has previously been shown to elicit specific phenotypes at high frequency and penetrance (55–60).

Phenotypic analysis of 3- to 4-d-old embryos (stage 42) injected at the one-cell stage showed prominent generalized edema in both *ift80*- and *ift172*-targeted embryos. Importantly, this phenotype was rescued by coinjecting *ift80* or *ift172* messenger RNA (mRNA), demonstrating the specificity of the sgRNA-mediated loss of function (Fig. 1 *A* and *B*). Morpholino oligonucleotide knockdown in *X. tropicalis* and CRISPR/Cas9 targeting elicited the same phenotype in *Xenopus laevis*, confirming the specificity of the phenotype in a separate species (*SI Appendix*, Fig. 1 *D* and *E*).

The most prominent phenotypes in chondrodysplasia patients are malformations of the axial skeleton and limbs [i.e., shortened ribs, long bone dysplasia, and polydactyly (4)]. Both *ift80* and *ift172* were expressed in limb buds (*SI Appendix*, Fig. 1*F*). Unilateral CRISPR targeting of F0 animals has been shown to be effective to disrupt genes essential for postmetamorphic limb development in *Xenopus* (61–63). To test if Ift80 and Ift172 act in limb development in *Xenopus*, we unilaterally injected two-cell–stage embryos, which limits gene editing to only one half of the body while retaining the unaffected half as an internal control. We targeted *slc45a2* as a negative control, which only results in a loss of pigmentation (59, 64). Apart from the expected loss of skin pigmentation, metamorphic froglets were phenotypically normal, demonstrating that sgRNA/Cas9 injection per se did not have an impact on development (Fig. 1*C*).

In contrast to control edited at the *ift80* or *ift172* locus showed severe limb defects. Both fore- and hindlimbs were substantially shorter than in control *slc45a2*-targeted froglets, as quantified in contrast enhanced micro-computed tomography (microCT) scans of mosaic mutant froglets (Fig. 1 *C*–*E*, green and red arrowheads). Despite unilateral RNP injections, we observed bilateral limb malformation in some animals, suggesting that in these cases, the first cell cleavage had not fully separated at the time of injection, allowing for gene editing to occur across the midline.

In most animals, the fingers and toes were shortened and less developed, sometimes not even identifiable (Fig. 1*C*). The number and size of clawed digits of the hindlimbs varied substantially from wild-types, in particular in *ift80*-targeted froglets (*SI Appendix*, Fig. 1*G*). *X. tropicalis* usually possess six digits at the hindlimb, four of which form claws (65). In *ift80*-targeted froglets, the number of clawed toes were consistently either reduced to less than three (syndactyly) or increased to six or seven (polydactyly) (Fig. 1*C*). In conclusion, this phenotype is highly reminiscent of the polydactyly phenotype observed in mouse models and human patients (24, 37, 40, 49, 66).

MicroCT images suggested that the shortened, not-yet-ossified limbs consisted mainly of cartilage accumulations (Fig. 1*C*, green arrowheads), consistent with the phenotype in humans and mouse models (48, 50, 67). Histological sections confirmed that the resting and proliferation zones of cartilage dominated clearly in *ift80*- and *ift172*-targeted animals at the expense of the hypertrophic and ossification zones visible in *slc45a2*-targeted control animals (Fig. 1*D*). In general, the chondrocytes were less well organized in *ift80*- and *ift172*-depleted cartilage than in limbs of controls. However, cartilage differentiation was unaffected in vertebrae, suggesting a limb-specific defect (*SI Appendix*, Fig. 2*A*).

Similar phenotypes have been described for conditional *ift80* knockout mice and other chondrodysplasia models (24, 26, 68–70).

Contrast-enhanced microCT was also able to resolve the structure of the mesonephric kidneys in the postmetamorphic froglets at high resolution and revealed polycystic kidneys in most of the mutant animals (Fig. 2 *A*–*C*). Quantification and volumetric analysis showed that both *ift80* and *ift172* disruption resulted in multiple cysts, particularly on the injected side (Fig. 2*D*). The occurrence of cysts on the uninjected side in *ift80* mosaic mutants likely reflects the incomplete segregation of gene editing to one

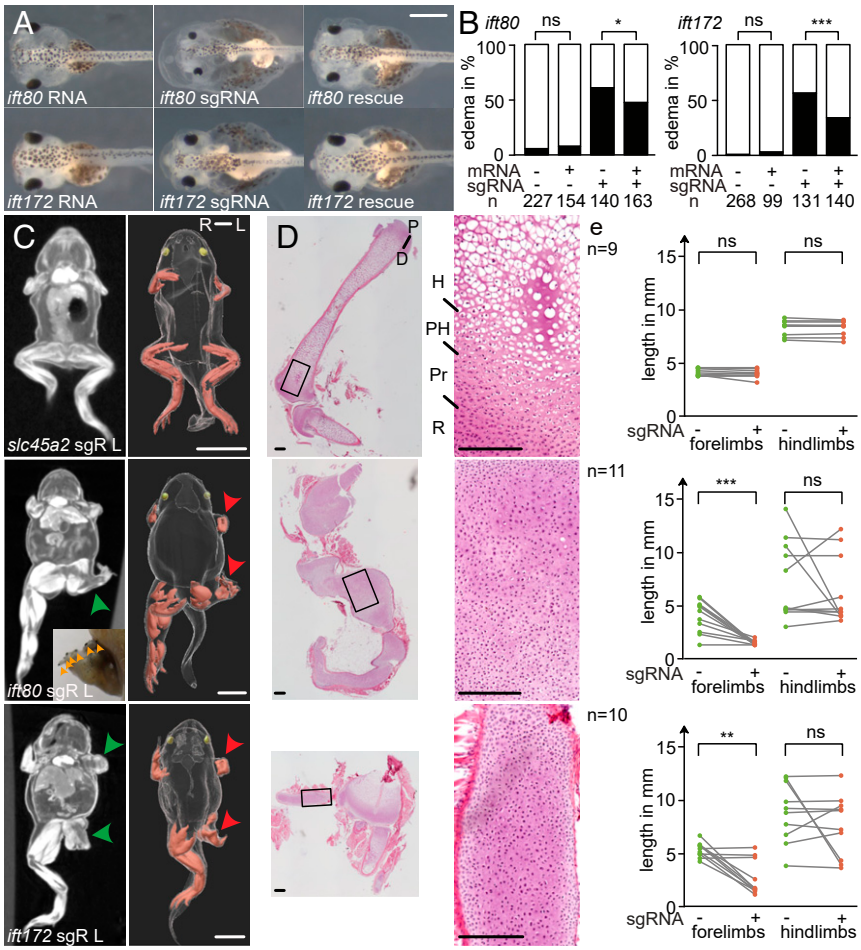

Fig. 1. CRISPR targeting of *ift80* and *ift172* leads to skeletal defects in *X. tropicalis*. (*A* and *B*) Analysis of edema formation in *ift80* and *ift172* crispants at stage 42. Note the smaller eyes in *ift80*-targeted embryos. (*C*) Limb phenotypes in postmetamorphic froglets (stage 62/63). MicroCT scans of representative crispant froglets of *slc45a2* (negative control), *ift80*, and *ift172* revealed cartilage accumulations in CRISPR-targeted froglets (green arrowheads). Injections of RNPs were performed unilaterally (*Left*) at the 2-cell stage. Polydactyly is indicated by orange arrowheads that mark black nailed digits. In the corresponding 3-dimensional reconstructions, limb muscles are shown in red, eyes in yellow, and red arrowheads point to the affected limbs. sgR L: left-sided sgRNA injection, R: right, L: left. (*D*) Histological sections of hindlimbs were stained with hematoxylin-eosin. R: resting zone; Pr: proliferating zone; PH: prehypertrophic zone; and H: hypertrophic zone. (*E*) The length of uninjected (green dots) versus injected (red dots) limbs of the same individual are plotted (gray lines). ns: (not significant); $*P < 0.05$; $**P < 0.01$; $***P < 0.001$. [Scale bars, (*A*) 0.5 mm, (*C*) 5 mm, and (*D*) 200 μm.]

half, as observed for limb measurements. The total cyst volume was significantly larger on the injected side of *ift80*-edited froglets (Fig. 2*E*), while the volume of noncystic renal parenchyma was not significantly different (Fig. 2*F*).

As ciliopathies can lead to retinal disease, we sectioned both embryo and froglet eyes for histological analysis. Apart from a mildly disorganized outer nuclear layer in *ift80*-targeted embryos, which may be due to the accompanying edema, we did not observe any obvious photoreceptor defects (*SI Appendix*, Fig. 2*B*). Likewise, no laterality defects were found (*SI Appendix*, Fig. 2 *C* and *D*).

We conclude that froglets with mutations in *ift80* and *ift172* displayed shortened extremities with polydactyly and cystic kidney disease, confirming that chondrodysplasia can be modeled in *Xenopus*. This supplements the available mouse and zebrafish lines and offers additional opportunities to analyze chondrodysplasia genes and their functions (49, 50, 67, 71).

***Ift80* and *ift172* Targeting Affects MCCs, Resulting in Pronephric Excretion Defects.** Next, we explored the effect of *ift80* and *ift172* disruption on a cellular level. The most prominent phenotype of *ift80* and *ift172* mutant tadpoles was generalized edema, suggesting a deficiency in water or ion homeostasis due to pronephric, lymphatic, vascular, or cardiac insufficiency. In situ hybridization of established marker genes (*aplnr*, vasculature; *nkx2.5*, heart; *prox1*, lymphatic system) did not reveal an obvious developmental disruption of any of these organ systems in *Xenopus* embryos targeted for *ift80* and *ift172* disruption (*SI Appendix*, Fig. 3 *C* and *D*). Given the prominent renal phenotype in froglets, the edema phenotype in embryos, and because Jeune syndrome patients and mouse models frequently suffer from kidney disease, we focused on the pronephros of *X. tropicalis* embryos (47). We did not find structural tubular defects when staining for the tubular epithelium (*SI Appendix*, Fig. 3 *E* and *F*) nor were the expression of segment-specific marker genes (*nkcc2*, distal tubule; *sglt1* proximal tubule) affected (*SI Appendix*, Fig. 3 *C* and *D*), suggesting a normal differentiation of tubular tissue.

Expression analysis of *ift80* and *ift172* by in situ hybridization revealed both genes to be prominently expressed in MCCs of the epidermis and nephrostomes (Fig. 2*G* and *SI Appendix*, Fig. 3 *A* and *B*). Nephrostomes are the most proximal tubular segments that facilitate uptake of coelomic fluid into the pronephric tubule (Fig. 2*H*). To test whether impaired fluid uptake into the tubule could explain the observed edema phenotype in *ift80* and *ift172* bilaterally disrupted embryos, we employed a dextran excretion

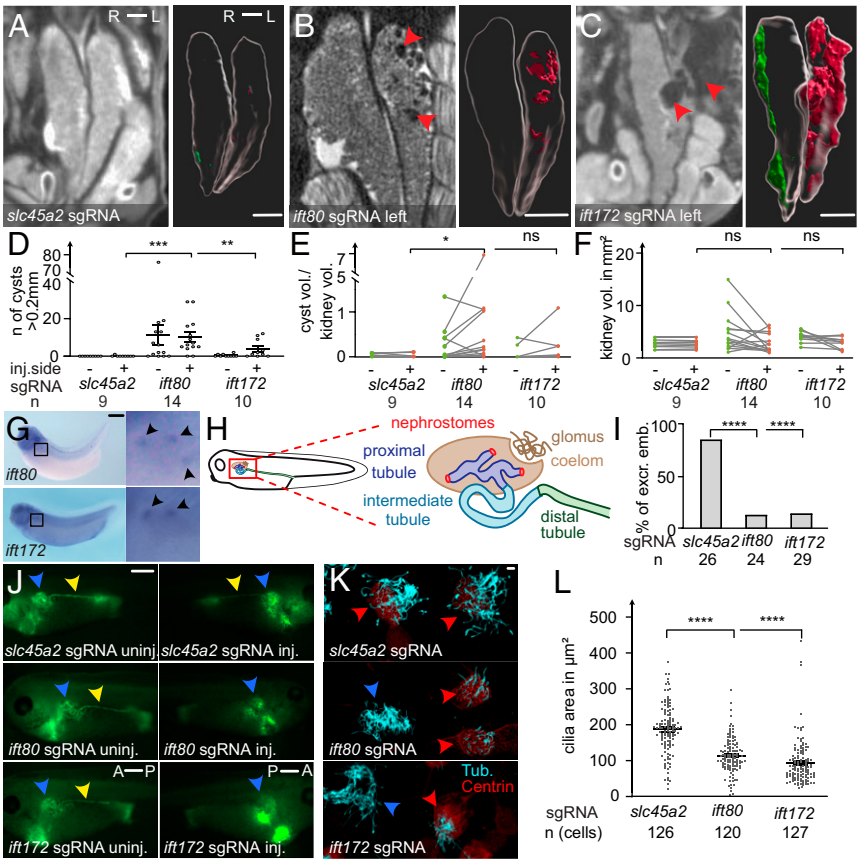

Fig. 2. Cystic kidney disease and cilia defects in *ift80* and *ift172* CRISPR–targeted *X. tropicalis*. (*A*–*C*) CRISPR/Cas9 targeting of *slc45a2*, *ift80*, and *ift172* were performed unilaterally in two-cell–stage embryos. Mesonephroi of stage 61 to 63 froglets were analyzed by microCT scans and kidneys and cysts (red arrowheads in *B* and *C*) were segmented for 3D volumetric analysis; red: cysts on the injected side; green: uninjected side). (*D*) The number of cysts (>0.2mm), (*E*) the ratio of total cyst volume to kidney volume, and (*F*) the kidney volume (excluding cysts) was calculated and compared with kidneys of control injected animals. (*G*) Whole-mount in situ hybridization detects *ift80* and *ift172* in the multiciliated nephrostomes of the pronephros in stage 36 to 38 *X. laevis*. (*H*) Schematic depiction of the embryonic renal system of *Xenopus*. (*I* and *J*) Excretion assay with fluorescein-dextran at stage 38 to 40. Blue arrowheads point to the proximal part of the pronephros. Yellow arrowheads indicate fluorescence signal in the distal tubule, lacking on the injected side (*J*). A: anterior, P: posterior; excr: excreting; and emb: embryos. (*K*) Confocal images of multiciliated epidermal cells (MCCs) stained against acetylated tubulin (cyan). Centrin-RFP fusion protein served as a lineage marker (red arrowheads) and indicates CRISPR-targeted MCCs. Blue arrowheads point to nontargeted (wild type) cells. (*L*) The ciliated area was determined for each cell. Error bars indicate SEM. $P > 0.05$ ns (not significant); $^{*}P < 0.05$; $^{**}P < 0.01$; $^{***}P < 0.001$. [Scale bars, (*A*–*C*) 1 mm, (*G* and *I*) 0.5 mm, and (*L*) 10 µm.]

assay. Embryos were injected with sgRNA/Cas9 at the two- to four-cell stage, and fluorescently labeled dextran was injected into the coelom at stage 39 to 40 when the pronephros is fully functional. Timelapse movies of *slc45a2* sgRNA–injected (negative control) embryos showed rapid uptake and acceleration of dextran through the pronephric tubule and excretion at the cloaca on both sides in 84.6% of embryos (Fig. 2 *I* and *J*). In contrast, entry into the pronephric tubule was observed in only 12.5 and 13.8% of embryos within 3 min on the *ift80*- and *ift172*-targeted side (Fig. 2 *I* and *J*), respectively. Dextran uptake was comparable to wild type and much faster on the nontargeted side of unilaterally gene-edited embryos. Normal excretion on the uninjected side could also be indirectly observed in the timelapse movies where dextran entered the medium of *ift80*- and *ift172*-targeted embryos (Movie 1).

Motile cilia in the nephrostomes actively propel fluid into the renal tubules. Thus, structural defects of ciliated cells may explain the observed loss of excretion in CRISPR-targeted tadpoles (45, 71). To analyze the role of *ift80* and *ift172* in motile cilia, we turned to the epidermal MCCs, a well-established and accessible model for ciliogenesis.

Centrin-red fluorescent protein mRNA was used as an injection marker to identify and label basal bodies of ciliated cells that had received the CRISPR RNPs, allowing us to analyze CRISPR-targeted and wild-type cells in the same images. Cilia appeared to be fewer and shorter in length, which was confirmed by quantification of cilia in *ift80* and *ift172* knockout cells (Fig. 2 *K* and *L*). In contrast, basal body number and apical docking was not altered in crispant MCCs when compared with controls (*SI Appendix*, Fig. 3*G*). Thus, the ciliogenesis defect is consistent with findings in other model organisms (45, 71) and a likely cause for impaired tubular uptake.

To gain more detailed insights into the molecular signals affected by a loss of *ift80* or *ift172*, we investigated the transcriptional profile of embryos targeted for *ift80* and *ift172*. Because embryos were in vitro fertilized and developed synchronously, stage-dependent variability was minimized between control and CRISPR-targeted embryos. We isolated DNA and confirmed a high indel frequency in the same samples subjected to RNA-Sequencing analysis at stage 22 (neurula) (*SI Appendix*, Fig. 4 *A* and *B*). The top-most down-regulated genes were *ift80* and *ift172*, respectively (*SI Appendix*, Fig. 4 *C*–*E* and Dataset S1), confirming the specificity of our targeting strategy and a direct effect on mRNA levels likely due to nonsense-mediated decay. We found 15 (*ift80*) and 5 (*ift172*) genes to be differentially regulated in either condition (*SI Appendix*, Fig. 4 *D* and *E*) and three genes (*abcb1* and two uncharacterized transcripts) to be significantly up-regulated in both conditions. The ATP-dependent multidrug-resistance transporter Abcb1 is transcriptionally

regulated by Gli1 and β-catenin (72, 73). Interestingly, an additional five genes that only reached significance in one condition were also associated with Hh signaling (*ccng1*, *ulk1*, *riok3*, *olfm4*, and *col1a1*) and four with Wnt signaling (*c3ar1*, *col1a1*, *olfm4*, and *ulk1*) (*SI Appendix*, Fig. 4*F*) (72, 74–82). Thus, we detect Hh- and Wnt-dependent gene regulation to be altered upon depletion of *ift80* and *ift172* in *Xenopus* embryos.

mRNA expression analysis in wild-type embryos of differentially regulated genes identified by RNA-Sequencing (*ccng1*, *ulk1*, and *riok3*) found an overlapping expression with chondrodysplasia genes in neuronal tissue and neural crest (*SI Appendix*, Fig. 4*G*). However, we did not find a change in the Sonic Hedgehog (Shh) marker *nkx2.2* after unilateral *ift80* or *ift172* targeting, suggesting that the differences in mRNA abundance are below the detection level of in situ hybridization (*SI Appendix*, Fig. 4 *H* and *I*).

Data Mining Identifies Skeletal Ciliopathy–Associated Genes. Next, we aimed to identify novel proteins related to the pathogenesis of SC. We reasoned that proteins with similar molecular properties, such as subcellular localization, common protein interactors, or differential regulation in loss-of-function models, could be unrecognized components of the pathogenetic molecular mechanism. Therefore, we assembled lists of genes from 90 published genome-wide screens or unbiased analyses ("resource lists") (Dataset S1) based on literature curation. We identified 16 resource lists to be significantly enriched for genetically validated chondrodysplasia genes in comparison with 10 million random draws of an equal number of query genes (Fig. 3*A*). Within these 16 lists, 65 unique genes not yet linked to chondrodysplasia were found to be significantly enriched (Dataset S1). Among these potential candidate genes were three that have been identified as bona fide chondrodysplasia genes in the meantime [i.e., *ift122*, *ift43*, and *traf3ip1* (70, 83, 84)]. *Ift22* was described to be mutated in a SRPS type IV patient, *ift43* and *traf3ip1* in SRPS type II patients, and *traf3ip1* additionally in a case of JATD (70, 83, 84). This confirmed that our approach was able to predict valid genetic associations.

Among the 65 potential chondrodysplasia-related candidate genes, we focused on the top four genes with the lowest *P* value that had not been linked to any ciliopathies nor characterized in a knockout mouse model and were targetable in *X. tropicalis* for functional analysis (*C11ORF74*, *CEP192*, *CFAP20*, and *TTC30B*; Fig. 3*B* and *SI Appendix*, Fig. 4*K*). All proteins encoded by these four candidate genes had previously been associated with cilia. CFAP20 (cilia- and flagella-associated protein 20) regulates cilia length and morphology (85, 86). Entering of the BBSome into the cilium via interaction with the IFT-A complex is controlled by C11ORF74 (87). CEP192 (centrosomal protein of 192 kDa) is required for mitotic centrosome and spindle assembly (88, 89). TTC30B (tetratricopeptide repeat domain 30b, also known as IFT70) is essential for polyglutamylation and polyglycylation of axonemal tubulin and is part of the IFT-B complex (90–92). *TTC30B* has one closely related homolog in humans (*TTC30A*) and three in mice (*Ttc30a1*, *Ttc30a2*, and *Ttc30b*) but only one ortholog in *X. tropicalis* and *Danio rerio* (*ttc30a/fleer*) (Fig. 4*A*) (91).

CRISPR/Cas9 Targeting *ttc30a* Replicates the Phenotype of *ift80*- and *ift172*-Targeted Embryos. We designed sgRNAs targeting all *Xenopus* orthologs of the four candidates for CRISPR/Cas9–mediated loss-of-function experiments. Interestingly, *cfap20* and *ttc30a* crispants formed edema suggestive of embryonic renal excretion defects. This effect was specific, as coinjection with corresponding mRNAs significantly rescued the edema phenotype (Fig. 4 *B* and *C* and *SI Appendix*, Fig. 5 *A–E*).

In order to evaluate a potential effect on limb development, we raised *cfap20*, *ttc30a*, *c11orf74*, and *cep192* CRISPR–targeted tadpoles to metamorphosis. Limb formation of *cep192*, *c11orf74*, and *cfap20* crispants was normal (*SI Appendix*, Fig. 5 *G* and *H*). Froglets with *ttc30a* mutations, however, developed severe limb defects (Fig. 4*D*, green arrowheads and *SI Appendix*, Fig. 5*F*). Extremities were generally shorter with polydactyly (Fig. 4*D* and *SI Appendix*, Fig. 5 *F* and *H*). MicroCT scans found large depositions of cartilage. Histology revealed a chondrocyte differentiation defect, as previously observed for *ift80*- and *ift172*-targeted animals. *Ttc30a*-targeted embryos had reduced fore- and hindlimb length (Fig. 4*D*), and analysis of the kidneys revealed a significantly higher number of cysts on the injected side of the froglets (Fig. 4*E*). However, total cyst and kidney volume did not change significantly (Fig. 4*E*). Excretion assays confirmed that renal tubular uptake of dextran was drastically reduced (Fig. 5 *A* and *B* and Movie 2), and epidermal cilia were shorter or absent in embryos injected with sgRNA and RNPs targeting *ttc30a* (Fig. 5 *C* and *D*). In conclusion, CRISPR targeting *ttc30a* in *Xenopus* replicated all phenotypes observed when targeting the chondrodysplasia genes *ift80* and *ift172*.

To elucidate the expression pattern of mammalian orthologs of *ttc30a*, we analyzed publicly available single-cell sequencing data of E13.5 mouse limb buds (*SI Appendix*, Fig. 6 *A–E*) (93). We found that among the three orthologs, *Ttc30b* and to a lesser degree *Ttc30a1* were most prominently expressed in cartilage, bone, and growth plate clusters (Fig. 5 *E–G*). The distribution of cell proportions expressing *Ttc30b* was similar to that of *Ift80* and *Ift172* (Fig. 5 *G* and *H*). Thus, the expression pattern of *Ttc30b* and *Ttc30a1* suggest a potential role in cartilage formation of mammals. We screened for *TTC30A/B* mutations in a cohort of 24 unresolved severe ciliary chondrodysplasia cases by exome sequencing, but no likely pathogenic variants were identified. Screening of whole-exome sequencing data in a worldwide cohort of more than 500 patients with nephronophthisis related ciliopathies and cystic kidney disease also did not reveal potentially causative recessive mutations in either *TTC30A* or *TTC30B*.

Ciliary Compartmentalization Is Altered in ttc30a- and ift172-Depleted Cilia. Ttc30a mediates tubulin modifications such as glycylation and glutamylation to be deposited within the ciliary axoneme (15, 91, 92).

Immunostaining with polyglutamylation- and monoglycylation-specific antibodies revealed that MCCs of the epidermis and in the nephrostomes were acetylated, glutamylated, and glycylated (Fig. 6 *A–D*). In contrast, ependymal MCCs positioned in the ventral neural tube were only glycylated but neither acetylated nor glutamylated (Fig. 6 *A* and *B*). All three analyzed modifications were also detected in primary cilia of the embryonic renal tubule cells. Closer inspection of the epidermal cilia revealed acetylated tubulin to be present in the entire axoneme and enhanced at the ciliary tip. Tubulin glycylation was present in the axoneme but spared the ciliary tip, while glutamylation was detected in a short proximal part of the axoneme (Fig. 6 *C* and *D*). Thus, posttranslational tubulin modifications distinguish cilia of various tissue cell types and compartmentalize the axoneme of individual cilia.

Targeting *ttc30a* by CRISPR/Cas9 injections revealed a reduction in the absolute and relative intensity of tubulin glycylation in relation to acetylation, used for normalization and segmentation of cilia (*SI Appendix*, Fig. 7 *A–C*). However, an increased glutamylation to acetylation index found in *ttc30a*- and *ift172*-depleted cilia was due to reduced axonemal acetylation, while glutamylation intensity was not changed (*SI Appendix*, Fig. 7 *D–F*). Closer inspection found that in *ttc30a*-, *ift80*-, and *ift172*-depleted cilia, the prominent acetylated tip was no longer present (Fig. 6 *C* and *D*), indicating defective axoneme compartmentalization.

Discussion

SC are caused by pathogenic mutations in genes that encode ciliary proteins. Thus, Mendelian genetics put the spotlight on the primary cilium as a central organelle in the pathophysiology of chondrodysplasias. This led to the insight that several clinically distinct disease entities may have a common molecular origin and are now recognized as a united disease group (4). Today, a

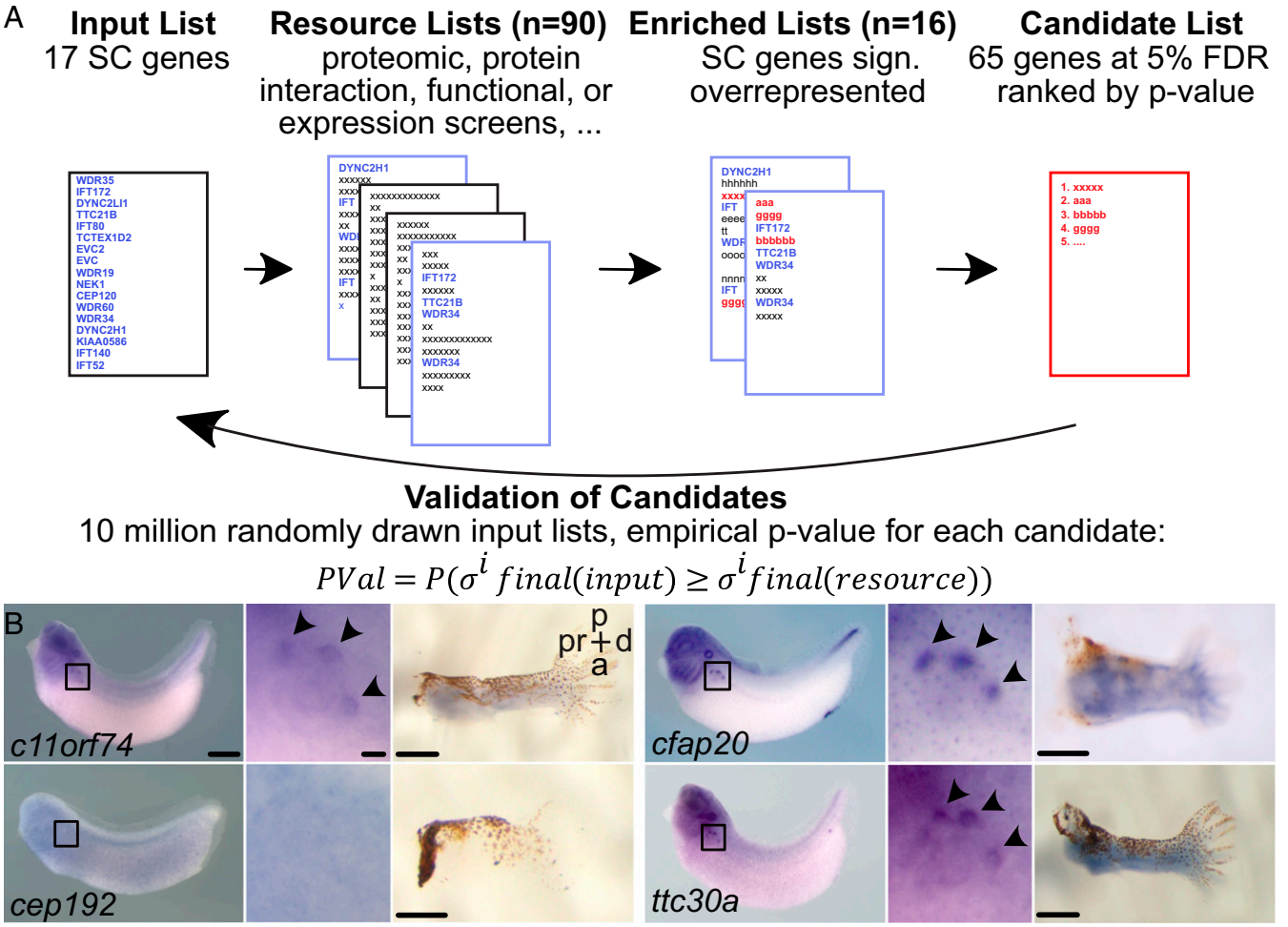

Fig. 3. In silico screening for candidates with similar properties to SC genes. (*A*) Schematic of the in silico screen. Known SC disease genes served as an input list. Resource lists represent datasets from various published screening approaches and were tested for enrichment of genes contained in the input list genes. Genes in significantly enriched resource lists were then scored based on membership or rank. The gene scores were statistically validated by an empirical *P* value based on 10 million random drawings of input list. (*B*) Whole-mount in situ hybridizations for four candidate genes (*c11orf74*, *cep192*, *cfap20*, and *ttc30a*) that were experimentally followed up are shown for tadpoles at stage 31 to 35 (nephrostome expression enlarged) and limb buds (stage 55 to 57). (Scale bars, 0.5 mm.) p, posterior; a, anterior; pr, proximal; and d, distal.

causative mutation can be found in almost all patients with SC, both in frequently affected genes and rare loci, which may only occur in a few patients worldwide.

Despite these enormous achievements, a full understanding of all disease-associated proteins, their functional relationships, and their molecular functions is incomplete. Therefore, novel in vivo models can help to assign tissue specific functions of ciliary proteins molecularly characterized in vitro. The tetrapod *X. tropicalis* is both easy to manipulate but not burdened by genome duplications that complicate genetic analysis in other aquatic models (94, 95). Thus, our work demonstrates that disruption of *Xenopus* orthologs of human SC disease genes elicit phenotypes highly consistent with the clinical presentation in patients and can be used to phenotypically validate novel chondrodysplasia candidate genes.

Early limb bud development in *Xenopus* is similar to that of other tetrapods on a molecular level (52, 96). An essential role of cilia and cilia-related signaling pathways (Hh and Wnt) is shaping cartilage and controlling bone size. Most SC genes have been described to influence Hh signaling (4). Shh defines the anterior–posterior axis and number of digits (96), while Indian hedgehog (Ihh) controls chondrocyte proliferation versus maturation in the growth plate and thus bone length (35, 97). As we observed phenotypes consistent with defects in Shh (polydactyly) and Ihh (brachydactyly), both pathways may be affected in our model (35, 36, 98). Interestingly, knockout mice of gpr161, a cilia-dependent regulator of both ligands, show a similar phenotype in forelimbs (99).

Wnt signaling has multiple functions during limb development, but it is not known to what degree Wnt signaling is affected in SC patients (100). Wnt/β-Catenin signaling acts in chondrocyte differentiation and is balanced by ift80 (48). Some SC genes have been linked to Wnt/PCP signaling, which affects the organization of chondrocytes (26, 27, 101, 102). Indeed, a combination of polysyndactyly and brachydactyly we observed is typical for a loss of *HOXD13*, which regulates *Shh* and *WNT5a* (Wnt/PCP) during limb development (101, 103, 104). A potential involvement of both, Wnt and Hh pathways, may explain why we detected changes in transcripts related to both signaling pathways (Fig. 3*A*).

A trove of existing datasets, proteomic, and functional screens have contributed to a better understanding of the protein composition of cilia (105, 106). Given that our data-mining approach worked well with chondrodysplasia genes, we used all gene sets annotated in phenotypic series in Online Mendelian Inheritance in Man (OMIM) as input. A significant number of enriched lists could be identified for 13 disease entities, many of which were ciliopathies (e.g., Meckel syndrome, nephronophthisis, and primary ciliary dyskinesia; Dataset S2). Interestingly, *TTC30A* was also included in the

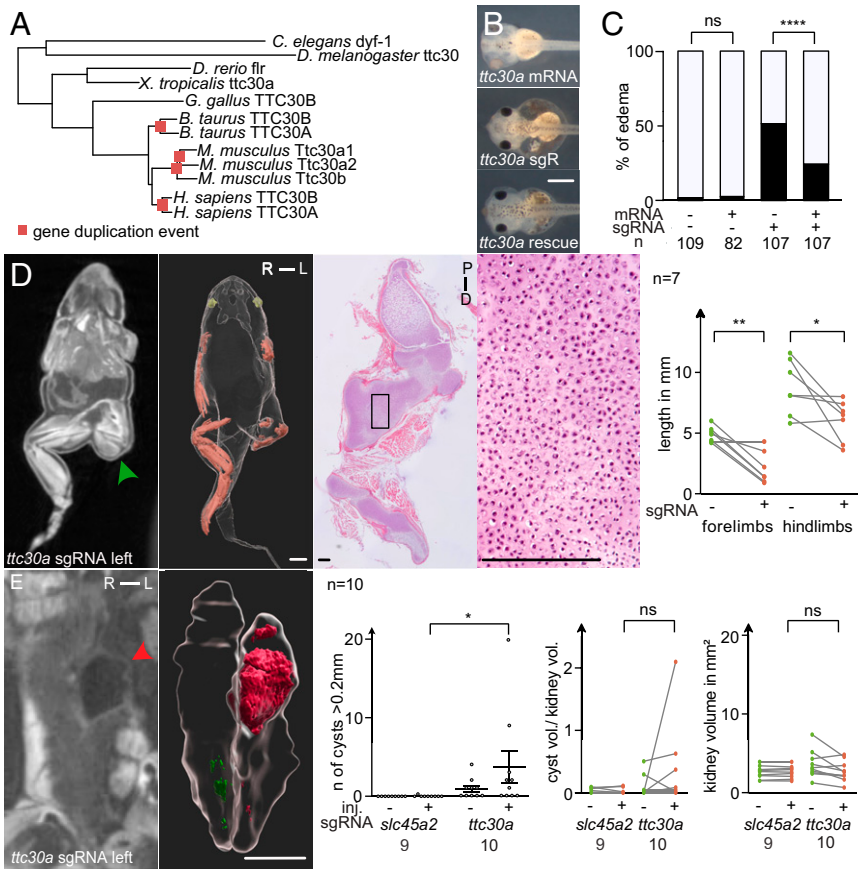

Fig. 4. *ttc30* loss of function resembles the SC-phenotype. (*A*) Phylogenetic tree of protein sequences of TTC30A/B orthologs in various species. Genetic duplication events are marked by red squares. (*B*) CRISPR targeting of *ttc30a* at the one-cell stage led to edema formation in stage 41 tadpoles, quantified in (*C*). Coinjection of *ttc30a* mRNA partially rescued the phenotype. (*D*) Unilaterally CRISPR-targeted *ttc30a* froglets developed shortened limbs on the injected side (green arrowhead). MicroCT analysis, 3D reconstructions, and histological sections stained with hematoxylin-eosin demonstrated accumulation of cartilage (green arrowhead). Quantification of limb length reduction of *ttc30a* targeted compared with nontargeted side. (*E*) MicroCT scans show cystic kidneys in *ttc30a*-targeted animals (red arrowhead). 3D reconstruction of the kidneys and cysts (red) were used for volumetric analysis. Quantifications of cyst number, the ratio of total cyst volume to kidney volume, and total kidney volume (excluding cysts). [Scale bars, (*B*) 0.5 mm, (*D* and *E*, 3D reconstruction) 2 mm, (*D*, histological section) 200 μm.] R, right; L, left; P, proximal; D, distal. $P > 0.05$ ns (not significant); *$P < 0.05$; **$P < 0.01$; ****$P < 0.0001$.

candidate-gene list for nephronophthisis. We created a web application to make the resource lists used in our in silico screen accessible and searchable (http://dormantdata.org). Adding further datasets and using novel machine learning algorithms may further enhance the power of a data-driven discovery process. Such refinements could make this approach applicable to other nonciliary diseases in the future or complement prioritization of potential pathogenic loci.

By in vivo modeling, we validated the in silico data and identified Ttc30a as a protein involved in chondrocyte differentiation and renal function. It is likely that not all SC-relevant components are known, and potentially deleterious variants may be too rare to be identified by Mendelian genetics because the natural mutational load does not reach saturation for all possible pathogenic mutations to occur or lead to early embryonic lethality. In addition, essential proteins may be protected by genetic compensation of functionally redundant genes (107, 108). The human *TTC30A/B* locus may represent a critical site that is protected by early and reoccurring duplication events in the tetrapod phylogeny that increasingly relied on limbs for locomotion and dexterity (Fig. 4*A*). TTC30A/B are highly conserved in eukaryotes. The amino acid sequence of the ortholog in *Chlamydomonas reinhardtii* and human TTC30A is 73% identical (90). In zebrafish, the *fleer* (*ttc30a*) mutant shows a general ciliopathy phenotype (91, 109). Cilia are either shorter or absent and lack parts of the microtubule duplets of the axoneme. Both in vitro and in vivo experiments identified ttc30a as a peripheral protein of the IFT-B1 subcomplex (110, 111), where it links the ift88/ift52-complex to Kif17 and mediates cargo interactions (Fig. 6 *E* and *F*) (112, 113). Furthermore, ttc30a is necessary for polyglutamylation and polyglycylation of tubulin by regulating the ciliary activity of ttll3/6 (Tubulin Tyrosine Ligase Like 3/6), and ccp5 (cytoplasmic carboxypeptidase 5; Fig. 6 *E* and *F*) (15, 92).

Both PTMs stabilize tubulin complexes and are necessary for cilia motility (92). Interestingly, polyglutamylation regulates velocity of the Kinesin-2 complex and therefore the uptake of Hh components (Smo and Gli3) after signaling activation and has recently been found to depend on the Joubert syndrome–associated proteins ARL13B and CEP41 (18, 19, 114). Loss of the Joubert syndrome–associated proteins ARMC9, TOGARAM1, and Kif7 also decreases acetylation (115). Knockout of Kif7 affects PTMs mainly at the tip of the cilium (116, 117). In our model, we find the strongest effect on tubulin glycylation and acetylation in the ciliary tip. On one hand, particle turnaround from anterograde to retrograde transport occurs at the tip, and ift172 is involved in this process (118). Furthermore, the tip is a crucial compartment for Hh-signaling molecule activation, which is disrupted in Kif7 knockout cells that also show decreased acetylation and glutamylation (117).

Our findings suggest that alterations of posttranslational tubulin modifications may contribute to the pathogenesis of ciliopathies

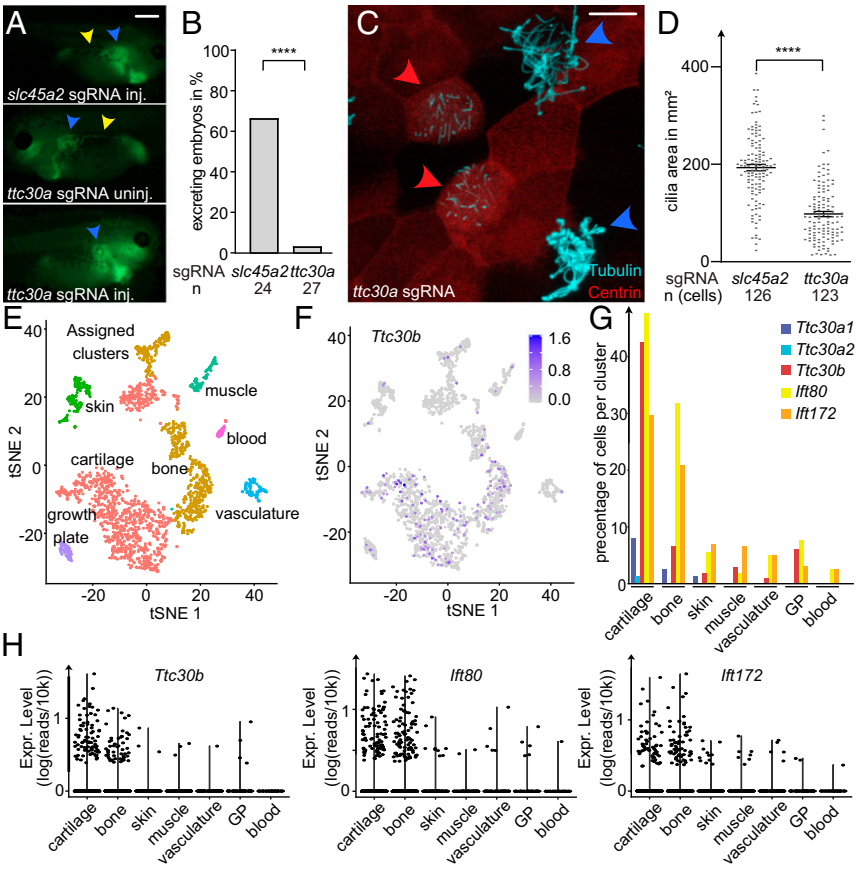

Fig. 5. Single cell RNA-Sequencing analysis of *Ttc30a/b*-positive cells in developing mouse limbs. (*A* and *B*) Excretion assay of *slc45a2* sgRNA–injected controls and *ttc30a*-targeted embryos. Blue arrowheads point to the proximal tubule, and yellow arrowheads highlight fluorescent dextran in the distal tubules as a measure of excretion. (*C*) Confocal images of epidermal MMCs of stage-36 embryos. centrin-RFP (red) marks cells targeted for *ttc30a* (red arrowheads). Blue arrowheads label wild-type cells. Cilia are stained with acetylated gamma-tubulin (cyan). (*D*) Quantification of ciliated area per cell in *slc45a2* and *ttc30a* CRISPR–targeted cells. Error bars indicate SEM. $P > 0.05$ ns (not significant); $*P < 0.05$; $**P < 0.01$; and $***P < 0.001$. (*E*) Clustering of scRNA-Seq data from E15.5 mouse limbs into 10 different cell clusters using typical marker genes. (*F*) Detection of *Ttc30b* expression in respective cell clusters. (*G*) Comparison of percentage of cells per cluster expressing *Ttc30a1*, *Ttc30a2*, *Ttc30b*, *Ift80*, and *Ift172*. (*H*) Expression level of *Ttc30b*, *Ift80*, and *Ift172* in respective tissue clusters. [Scale bars, (*A*) 0.5 mm and (*C*) 10 μm.] GP, growth plate.

beyond Joubert syndrome, such as chondrodysplasia and nephronophthisis. Intriguingly, the ciliary localization of PKD2 was found to depend on tubulin glutamylation, suggesting a potential role in renal cystogenesis (18, 119).

Like glutamylation, tubulin glycylation appears to be present only in primary cilia of certain cell types. Glycylation was detected in Madin-Darby Canine Kidney (MDCK) cells but absent in mouse inner medullary collecting duct (mIMCD3) and human retinal pigment epithelial (RPE-1) cells (16). Only a subset of cilia in the zebrafish spinal cord and pronephros are glycylated, but none in Kupffer's vesicle (92). We found that motile cilia in the neural tube and nephrostomes were glycylated but not primary cilia in pronephric tubules. In contrast, both types of cilia are glutamylated. Spinal cord cilia were neither acetylated nor glutamylated but only glycylated. Thus, tubulin amino acid PTMs not only constitute a part of the "tubulin code" that diversifies ciliary functions, but its disruption may contribute to the pleiotropic phenotypes of ciliopathies (119).

TTC30A/B are known ciliary components but have not been associated with skeletal defects. In human tissue, TTC30A and TTC30B are strongly expressed in mammalian ciliated tissues, such as airway epithelia or ductuli efferentes in the epididymis (120). Consistent with our own analysis, single-cell RNA-Sequencing data of embryonic mice revealed an enhanced expression of *ttc30a1*, *ttc30a2*, and *ttc30b* in osteoblasts and chondrocytes (Fig. 5 *E–H*) (121). A rare missense variant in *TTC30B* (rc.1157C > T, p.A375V) has recently been described in a large Chinese family with polysyndactyly, suggesting an autosomal-dominant mode of inheritance (122). However, no other unifying clinical phenotypes were observed in the 27 affected family members. In vitro analysis suggested that down-regulation of *TTC30B* had an inhibitory effect on Shh-pathway stimulation, consistent with our findings that Ttc30a has a role in limb patterning. Hh signaling does not influence cystogenesis in autosomal polycystic kidney disease, suggesting that other ciliary mechanisms are more likely to be at play (123). Further investigation will need to elucidate which signals are disrupted by loss of Ttc30a in renal cyst formation and which other molecular signals are affected by disrupted posttranslational tubulin modifications and defective ciliary compartmentalization. These insights will be essential to improve the understanding of the pathogenesis of nephronophthisis, ciliary chondrodysplasia, and other ciliopathies.

Materials and Methods

Animal Maintenance and Handling. Adult animals were kept according to the German and Swiss law for care and handling of research animals. Husbandry and treatment were approved by the local authorities (Regierungspräsidium Freiburg and Veterinäramt Zürich).

Microinjections. Embryos were obtained by in vitro fertilization (*X. laevis* and *X. tropicalis*) or natural mating (*X. tropicalis*). For injections, embryos were

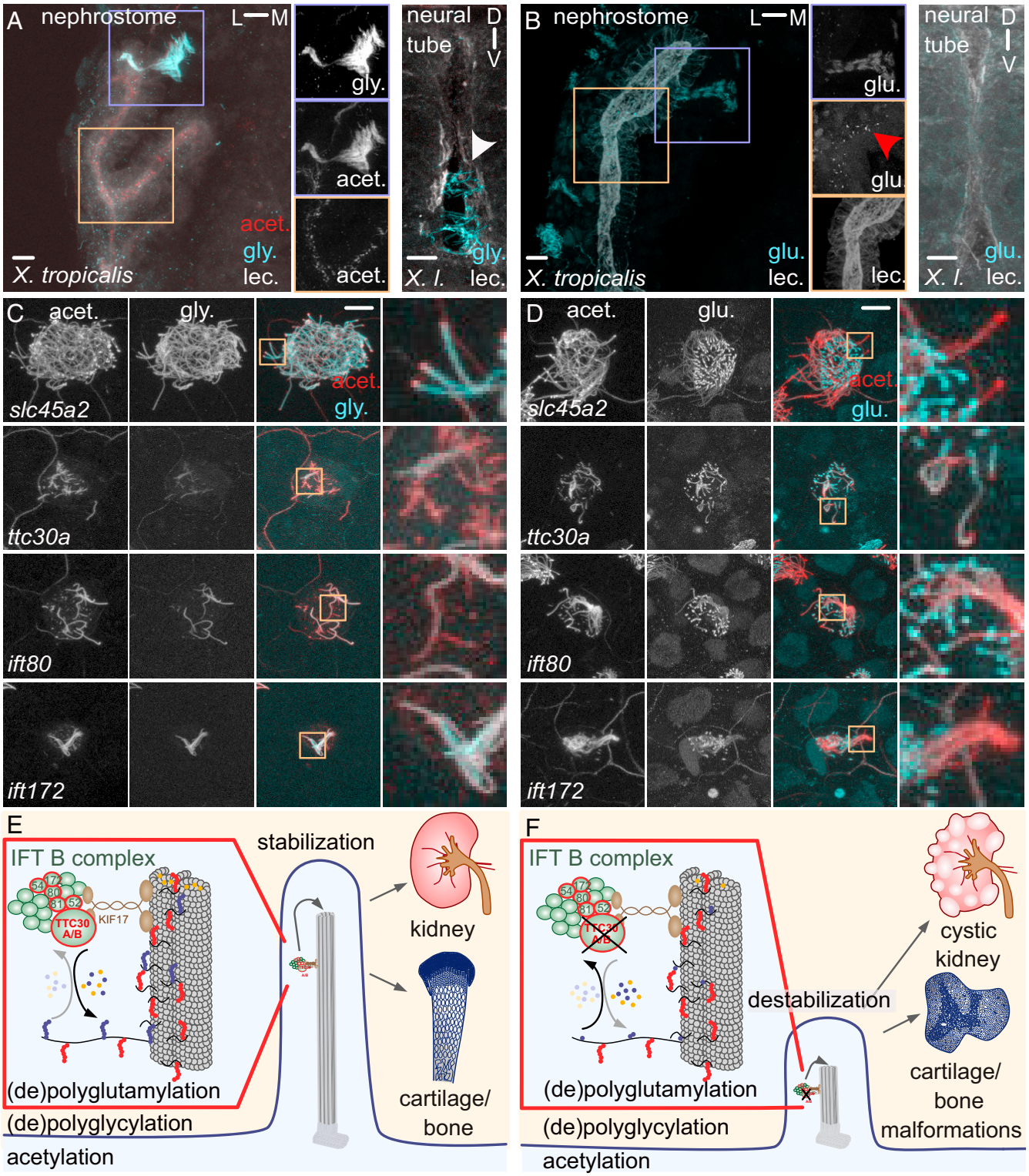

Fig. 6. Ttc30a affects posttranslational tubulin modifications and ciliary compartmentalization. (*A*) Glycylation (cyan) in combination with acetylation (red) and (*B*) glutamylation (cyan) of pronephric and neural tube cilia were detected by immunostaining in wild-type embryos at stage 39. Cells of the pronephros and neural tube were visualized by Lectin staining (white/gray). White arrowhead points to ventral cilia of the neural tube, and red arrowhead to primary cilia of the pronephric tubular system. Stainings of the nephrostomes and tubular system are also shown as single channels. L, lateral; M, medial; D, dorsal; V, ventral; gly, glycylation; lec, lectin; glu, glutamylation; and acet, acetylation. Influence of targeting *ift80*, *ift172*, and *ttc30a* by CRISPR/Cas9 on glycylation (*C*) and glutamylation (*D*) was analyzed by immunostainings of epidermal cilia at stage 36 (glutamylation/glycylation, cyan; acetylation, red). (*E* and *F*) A schematic model for the role of ttc30a during bone and kidney development. (*E*) Ttc30a interacts with Kif17 in the cilium and is crucial for tubulin modifications (blue, glycylation; red, glutamylation; and yellow, acetylation) (15, 92, 112). Mutations of *ttc30a* in *Xenopus* reduce acetylation and glycylation, negatively impact cartilage differentiation, and result in kidney cysts (*F*). Green, intraflagellar transport (IFT)-B proteins; red circled, known SC genes; gray, ciliary tubulin. Error bars indicate SEM. $P > 0.05$ ns (not significant); $^{*}P < 0.05$; $^{**}P < 0.01$; and $^{***}P < 0.001$. (Scale bars, 10 μm.)

transferred to 3% Ficoll with 0.1% bovine serum albumin (*X. tropicalis*) or 2% Ficoll (*X. laevis*) dissolved in 0.3× Marc's Modified Ringer's. Depending on the experiment embryos were injected at the 1-cell stage (phenotype analysis, genotyping, and RNA-Sequencing) or unilaterally at 2- to 4-cell stage (all other experiments). The injected volume was 10 nL in *X. laevis* and 5 nL in *X. tropicalis*. In all experiments, a lineage tracer was coinjected, and embryos were sorted according to the injected side at neurula stage.

Analysis of CRISPR/Cas9 Froglets. Froglets for limb analysis were euthanized and fixed in MOPS pH 7.4, 2 mM EGTA, 1 mM MgSO4, 3.7% formaldehyde (MEMFA). Iodine contrast enhancement was done by washing froglets in 1× phosphate-buffered saline for 2 d, followed by dehydration to ethanol, and staining in 1% iodine solution (Sigma-Aldrich, 207772) in ethanol. After washing with 100% ethanol, the animals were scanned with a Caliper Quantum Fx from PerkinElmer. Imaris 9.5.1 was used to determine the volume of kidneys and kidney cysts. The length of limbs was measured with RadiAnt DICOM Viewer 5.5.1. To determine the total length of the hindlimb, length of femur and tibia/fibula was measured and summed. The length of forelimbs was determined by adding the length of humerus and ulna/radius.

In Silico Screen to Identify SC Candiates. For the in silico screen, we performed PubMed searches for the terms "cilia" or "ciliogenesis" and manually identified 90 datasets that were part of publications related to cilia or ciliogenesis in various species that contained genome-, transcriptome-, or proteome-wide analysis. These resource lists were classified as ranked or unranked and critical parameters used as a basis for the statistical analysis by two independent annotators (resource lists, Dataset S1).

Because these lists were obtained from screening experiments in multiple species, all gene identifiers were matched to the closest human ortholog. Gene names were mapped to the human ortholog (HGNC) using biomart and manually curated. OMIM "phenotypic series" data were aggregated from the genemap.txt file downloaded on 26.01.2017 to obtain the 388 input lists of known and confirmed genetic diseases by matching phenotype descriptions to gene symbols.

First, each resource list was tested by Fisher's exact test, in which multiple testing was accounted for by use of a Bonferroni correction for the number or resource lists, to determine if the genes in the input list were enriched ($P < 0.05/90$) in a given resource list (124). Genes on resource lists that showed significant enrichment of known monogenic genes on input lists were scored according to either their position in ranked resource lists ($\sigma_{ranked} = rank^{-1} / \sum^{ranks}$) or by the total number of genes in the resource list ($\sigma_{unranked} = 1 / (length\ (list))$). Then, combined scores across all enriched resource lists were computed. Finally, we drew 10 million random input lists and scored genes analogously to estimate the background distribution of scores, compute resampling based enrichment *P* values and to adjust for multiple testing by the Benjamini–Hochberg procedure (false discovery rate < 0.05).

Data Availability. All study data are included in the article and/or supporting information. The raw data associated with *SI Appendix*, Fig. 4 *C–E* was deposited at the Sequence Read Archive (SRA) with the BioProject accession number PRJNA670560 (125). The code used in the in silico screen is publicly available at GitHub, https://github.com/genepi-freiburg/GeneSet (126).

ACKNOWLEDGMENTS. We are grateful for technical assistance from Alena Sammarco, Jessika Kleindienst, Marko Vujanovic, Claudia Meyer, the staff of the Life Imaging Center Freiburg at the Center for Biological Systems Analysis of the University of Freiburg, the Center for Microscopy and Image Analysis, and the Zurich Integrative Rodent Physiology of the University of Zurich. This study was supported by the German Research Foundation to S.S.L. (Emmy Noether Program Li-Li 1817/2-1), P.S. (Project ID 192904750–CRC 992 Medical Epigenetics), A.K. (KO 3598-5/1; Project-ID 431984000–SFB 1453 Nephrogenetics and Centre for Integrative Biological Signalling CIBSS–EXC-2189–Project ID 390939984), and E.L. (Project-ID 431984000–SFB1453 Nephrogenetics), the European Union's Horizon 2020 research and innovation programme to E.L. (MCDS-Therapy Grant Agreement No. 754825) and S.S.L. (DiRECT Grant Agreement No. 804474), the EQUIP Program for Medical Scientists, Faculty of Medicine, University of Freiburg to P.S., the NIH (No. R01DK068306) to F. Hildebrandt, and the Swiss National Science Foundation to S.S.L. (National Centre of Competence in Research NCCR Kidney.CH) and (Project ID 310030_189102/1).

1. C. Kempeneers, M. A. Chilvers, To beat, or not to beat, that is question! The spectrum of ciliopathies. *Pediatr. Pulmonol.* **53**, 1122–1129 (2018).
2. D. A. Braun, F. Hildebrandt, Ciliopathies. *Cold Spring Harb. Perspect. Biol.* **9**, a028191 (2017).
3. H. Y. Chen, R. A. Kelley, T. Li, A. Swaroop, Primary cilia biogenesis and associated retinal ciliopathies. *Semin. Cell Dev. Biol.* **110**, 70–88. (2021).
4. M. Schmidts, H. M. Mitchison, "Severe skeletal abnormalities caused by defects in retrograde intraflagellar transport dyneins" in *Dyneins*, S. King, Ed. (Elsevier, 2018), 356–401.
5. M. V. Nachury *et al.*, A core complex of BBS proteins cooperates with the GTPase Rab8 to promote ciliary membrane biogenesis. *Cell* **129**, 1201–1213 (2007).
6. S. Hoff *et al.*, ANKS6 is a central component of a nephronophthisis module linking NEK8 to INVS and NPHP3. *Nat. Genet.* **45**, 951–956 (2013).
7. A. Handa, U. Voss, A. Hammarsjö, G. Grigelioniene, G. Nishimura, Skeletal ciliopathies: A pattern recognition approach. *Jpn. J. Radiol.* **38**, 193–206 (2020).
8. K. A. Geister, S. A. Camper, Advances in skeletal dysplasia genetics. *Annu. Rev. Genomics Hum. Genet.* **16**, 199–227 (2015).
9. Schmidts, M. Clinical genetics and pathobiology of ciliary chondrodysplasias. *J. Pediatr. Genet.* **3**, 49–64 (2015).
10. M. A. Aldahmesh *et al.*, IFT27, encoding a small GTPase component of IFT particles, is mutated in a consanguineous family with Bardet-Biedl syndrome. *Hum. Mol. Genet.* **23**, 3307–3315 (2014).
11. A. Lindstrand *et al.*, Copy-number variation contributes to the mutational load of Bardet-Biedl syndrome. *Am. J. Hum. Genet.* **99**, 318–336 (2016).
12. D. U. Mick *et al.*, Proteomics of primary cilia by proximity labeling. *Dev. Cell* **35**, 497–512 (2015).
13. P. Kohli *et al.*, The ciliary membrane-associated proteome reveals actin-binding proteins as key components of cilia. *EMBO Rep.* **18**, 1521–1535 (2017).
14. H. Ishikawa, J. Thompson, J. R. Yates III, W. F. Marshall, Proteomic analysis of mammalian primary cilia. *Curr. Biol.* **22**, 414–419 (2012).
15. N. Pathak, C. A. Austin-Tse, Y. Liu, A. Vasilyev, I. A. Drummond, Cytoplasmic carboxypeptidase 5 regulates tubulin glutamylation and zebrafish cilia formation and function. *Mol. Biol. Cell* **25**, 1836–1844 (2014).
16. S. Gadadhar *et al.*, Tubulin glycylation controls primary cilia length. *J. Cell Biol.* **216**, 2701–2713 (2017).
17. A. Roll-Mecak, The tubulin code in microtubule dynamics and information encoding. *Dev. Cell* **54**, 7–20 (2020).
18. K. He *et al.*, Axoneme polyglutamylation regulated by Joubert syndrome protein ARL13B controls ciliary targeting of signaling molecules. *Nat. Commun.* **9**, 3310 (2018).
19. J. E. Lee *et al.*, CEP41 is mutated in Joubert syndrome and is required for tubulin glutamylation at the cilium. *Nat. Genet.* **44**, 193–199 (2012).
20. D. Huangfu *et al.*, Hedgehog signalling in the mouse requires intraflagellar transport proteins. *Nature* **426**, 83–87 (2003).
21. A. Liu, B. Wang, L. A. Niswander, Mouse intraflagellar transport proteins regulate both the activator and repressor functions of Gli transcription factors. *Development* **132**, 3103–3111 (2005).
22. A. N. Hoover *et al.*, C2cd3 is required for cilia formation and Hedgehog signaling in mouse. *Development* **135**, 4049–4058 (2008).
23. R. W. Stottmann, P. V. Tran, A. Turbe-Doan, D. R. Beier, Ttc21b is required to restrict sonic hedgehog activity in the developing mouse forebrain. *Dev. Biol.* **335**, 166–178 (2009).
24. S. Rix, A. Calmont, P. J. Scambler, P. L. Beales, An Ift80 mouse model of short rib polydactyly syndromes shows defects in hedgehog signalling without loss or malformation of cilia. *Hum. Mol. Genet.* **20**, 1306–1314 (2011).
25. A. M. McInerney-Leo *et al.*; UK10K Consortium, Short-rib polydactyly and Jeune syndromes are caused by mutations in WDR60. *Am. J. Hum. Genet.* **93**, 515–523 (2013).
26. S. Paige Taylor *et al.*; University of Washington Center for Mendelian Genomics, An inactivating mutation in intestinal cell kinase, *ICK*, impairs hedgehog signalling and causes short rib-polydactyly syndrome. *Hum. Mol. Genet.* **25**, 3998–4011 (2016).
27. S. P. Taylor *et al.*; University of Washington Center for Mendelian Genomics Consortium, Mutations in DYNC2LI1 disrupt cilia function and cause short rib polydactyly syndrome. *Nat. Commun.* **6**, 7092 (2015).
28. C. Wu *et al.*, Talpid3-binding centrosomal protein Cep120 is required for centriole duplication and proliferation of cerebellar granule neuron progenitors. *PLoS One* **9**, e107943 (2014).
29. J. A. Caparrós-Martín *et al.*, The ciliary Evc/Evc2 complex interacts with Smo and controls Hedgehog pathway activity in chondrocytes by regulating Sufu/Gli3 dissociation and Gli3 trafficking in primary cilia. *Hum. Mol. Genet.* **22**, 124–139 (2013).
30. C. Alby *et al.*, Mutations in KIAA0586 cause lethal ciliopathies ranging from a hydrolethalus phenotype to short-rib polydactyly syndrome. *Am. J. Hum. Genet.* **97**, 311–318 (2015).
31. C. Wu, J. Li, A. Peterson, K. Tao, B. Wang, Loss of dynein-2 intermediate chain Wdr34 results in defects in retrograde ciliary protein trafficking and Hedgehog signaling in the mouse. *Hum. Mol. Genet.* **26**, 2386–2397 (2017).
32. K. M. Frikstad *et al.*, A CEP104-CSPP1 complex is required for formation of primary cilia competent in hedgehog signaling. *Cell Rep.* **28**, 1907–1922.e6 (2019).
33. Z. Anvarian, K. Mykytyn, S. Mukhopadhyay, L. B. Pedersen, S. T. Christensen, Cellular signalling by primary cilia in development, organ function and disease. *Nat. Rev. Nephrol.* **15**, 199–219 (2019).
34. F. Bangs, K. V. Anderson, Primary cilia and mammalian hedgehog signaling. *Cold Spring Harb. Perspect. Biol.* **9**, a028175 (2017).

35. B. St-Jacques, M. Hammerschmidt, A. P. McMahon, Indian hedgehog signaling regulates proliferation and differentiation of chondrocytes and is essential for bone formation. *Genes Dev.* **13**, 2072–2086 (1999).
36. Y. Litingtung, R. D. Dahn, Y. Li, J. F. Fallon, C. Chiang, Shh and Gli3 are dispensable for limb skeleton formation but regulate digit number and identity. *Nature* **418**, 979–983 (2002).
37. D. P. Cavalcanti *et al*., Mutation in IFT80 in a fetus with the phenotype of Verma-Naumoff provides molecular evidence for Jeune-Verma-Naumoff dysplasia spectrum. *J. Med. Genet.* **48**, 88–92 (2011).
38. V. Bizaoui *et al*., Mutations in *IFT80* cause SRPS Type IV. Report of two families and review. *Am. J. Med. Genet. A.* **179**, 639–644 (2019).
39. P. L. Beales *et al*., IFT80, which encodes a conserved intraflagellar transport protein, is mutated in Jeune asphyxiating thoracic dystrophy. *Nat. Genet.* **39**, 727–729 (2007).
40. J. Halbritter *et al*.; UK10K Consortium, Defects in the IFT-B component IFT172 cause Jeune and Mainzer-Saldino syndromes in humans. *Am. J. Hum. Genet.* **93**, 915–925 (2013).
41. E. Schaefer *et al*., Identification of a novel mutation confirms the implication of IFT172 (BBS20) in Bardet-Biedl syndrome. *J. Hum. Genet.* **61**, 447–450 (2016).
42. K. M. Bujakowska *et al*., Mutations in IFT172 cause isolated retinal degeneration and Bardet-Biedl syndrome. *Hum. Mol. Genet.* **24**, 230–242 (2015).
43. M. Taschner *et al*., Intraflagellar transport proteins 172, 80, 57, 54, 38, and 20 form a stable tubulin-binding IFT-B2 complex. *EMBO J.* **35**, 773–790 (2016).
44. Y. Katoh *et al*., Overall architecture of the intraflagellar transport (IFT)-B complex containing Cluap1/IFT38 as an essential component of the IFT-B peripheral subcomplex. *J. Biol. Chem.* **291**, 10962–10975 (2016).
45. L. M. Hudak *et al*., The intraflagellar transport protein ift80 is essential for photoreceptor survival in a zebrafish model of jeune asphyxiating thoracic dystrophy. *Invest. Ophthalmol. Vis. Sci.* **51**, 3792–3799 (2010).
46. M. Gorivodsky *et al*., Intraflagellar transport protein 172 is essential for primary cilia formation and plays a vital role in patterning the mammalian brain. *Dev. Biol.* **325**, 24–32 (2009).
47. J. M. Friedland-Little *et al*., A novel murine allele of intraflagellar transport protein 172 causes a syndrome including VACTERL-like features with hydrocephalus. *Hum. Mol. Genet.* **20**, 3725–3737 (2011).
48. X. Yuan *et al*., Ciliary IFT80 balances canonical versus non-canonical hedgehog signalling for osteoblast differentiation. *Nat. Commun.* **7**, 11024 (2016).
49. P. W. Howard, T. L. Howard, R. A. Maurer, Generation of mice with a conditional allele for Ift172. *Transgenic Res.* **19**, 121–126 (2010).
50. X. Li, S. Yang, L. Han, K. Mao, S. Yang, Ciliary IFT80 is essential for intervertebral disc development and maintenance. *FASEB J.* **34**, 6741–6756 (2020).
51. K. Shimizu-Nishikawa, J. Takahashi, A. Nishikawa, Intercalary and supernumerary regeneration in the limbs of the frog, *Xenopus laevis*. *Dev. Dyn.* **227**, 563–572 (2003).
52. B. Christen, A. M. C. Rodrigues, M. B. Monasterio, C. F. Roig, J. C. Izpisua Belmonte, Transient downregulation of Bmp signalling induces extra limbs in vertebrates. *Development* **139**, 2557–2565 (2012).
53. F. Wang *et al*., Targeted gene disruption in *Xenopus laevis* using CRISPR/Cas9. *Cell Biosci.* **5**, 15 (2015).
54. G. F. Stopper, K. L. Richards-Hrdlicka, G. P. Wagner, Hedgehog inhibition causes complete loss of limb outgrowth and transformation of digit identity in *Xenopus tropicalis*. *J. Exp. Zoolog. B Mol. Dev. Evol.* **326**, 110–124 (2016).
55. R. S. Wu *et al*., A rapid method for directed gene knockout for screening in G0 zebrafish. *Dev. Cell* **46**, 112–125.e4 (2018).
56. K. Hoshijima *et al*., Highly efficient CRISPR-Cas9-based methods for generating deletion mutations and F0 embryos that lack gene function in zebrafish. *Dev. Cell* **51**, 645–657.e4 (2019).
57. L.-E. Jao, S. R. Wente, W. Chen, Efficient multiplex biallelic zebrafish genome editing using a CRISPR nuclease system. *Proc. Natl. Acad. Sci. U.S.A.* **110**, 13904–13909 (2013).
58. M. Banach, E.-S. Edholm, J. Robert, Exploring the functions of nonclassical MHC class Ib genes in *Xenopus laevis* by the CRISPR/Cas9 system. *Dev. Biol.* **426**, 261–269 (2017).
59. B. D. DeLay *et al*., Tissue-specific gene inactivation in *Xenopus laevis*: Knockout of *lhx1* in the kidney with CRISPR/Cas9. *Genetics* **208**, 673–686 (2018).
60. I. L. Blitz, J. Biesinger, X. Xie, K. W. Y. Cho, Biallelic genome modification in F0 Xenopus tropicalis embryos using the CRISPR/Cas system. *genesis* **51**, 827–834 (2013).
61. T. Naert *et al*., CRISPR/Cas9 mediated knockout of rb1 and rbl1 leads to rapid and penetrant retinoblastoma development in *Xenopus tropicalis*. *Sci. Rep.* **6**, 35264 (2016).
62. E. Szenker-Ravi *et al*., RSPO2 inhibition of RNF43 and ZNRF3 governs limb development independently of LGR4/5/6. *Nature* **557**, 564–569 (2018).
63. A. Kariminejad *et al*., Homozygous null TBX4 mutations lead to posterior amelia with pelvic and pulmonary hypoplasia. *Am. J. Hum. Genet.* **105**, 1294–1301 (2019).
64. M. Shigeta *et al*., Rapid and efficient analysis of gene function using CRISPR-Cas9 in *Xenopus tropicalis* founders. *Genes Cells* **21**, 755–771 (2016).
65. S. Hayashi *et al*., Evidence for an amphibian sixth digit. *Zoological Lett.* **1**, 17 (2015).
66. I. Casteels, E. Demandt, E. Legius, Visual loss as the presenting sign of Jeune syndrome. *Eur. J. Paediatr. Neurol.* **4**, 243–247 (2000).
67. X. Yuan, S. Yang, Primary cilia and intraflagellar transport proteins in bone and cartilage. *J. Dent. Res.* **95**, 1341–1349 (2016).
68. X. Yuan, S. Yang, Deletion of IFT80 impairs epiphyseal and articular cartilage formation due to disruption of chondrocyte differentiation. *PLoS One* **10**, e0130618 (2015).
69. I. Duran *et al*., Destabilization of the IFT-B cilia core complex due to mutations in IFT81 causes a spectrum of short-rib polydactyly syndrome. *Sci. Rep.* **6**, 34232 (2016).
70. I. Duran *et al*., Mutations in IFT-A satellite core component genes *IFT43* and *IFT121* produce short rib polydactyly syndrome with distinctive campomelia. *Cilia* **6**, 7 (2017).
71. S. C. Lunt, T. Haynes, B. D. Perkins, Zebrafish *ift57, ift88*, and *ift172* intraflagellar transport mutants disrupt cilia but do not affect hedgehog signaling. *Dev. Dyn.* **238**, 1744–1759 (2009).
72. J. Sims-Mourtada, J. G. Izzo, J. Ajani, K. S. C. Chao, Sonic Hedgehog promotes multiple drug resistance by regulation of drug transport. *Oncogene* **26**, 5674–5679 (2007).
73. S. Corrêa *et al*., *ABCB1* regulation through LRPPRC is influenced by the methylation status of the GC -100 box in its promoter. *Epigenetics* **9**, 1172–1183 (2014).
74. Y. Chen, M. M. Bieber, N. N. H. Teng, Hedgehog signaling regulates drug sensitivity by targeting ABC transporters ABCB1 and ABCG2 in epithelial ovarian cancer. *Mol. Carcinog.* **53**, 625–634 (2013).
75. J. Sun *et al*., The effects of Indian hedgehog deletion on mesenchyme cells: Inducing intermediate cartilage scaffold ossification to cause growth plate and phalange joint absence, short limb, and dwarfish phenotypes. *Stem Cells Dev.* **27**, 1412–1425 (2018).
76. H. Li *et al*., Olfactomedin 4 deficiency promotes prostate neoplastic progression and is associated with upregulation of the hedgehog-signaling pathway. *Sci. Rep.* **5**, 16974 (2015).
77. M. Tariki *et al*., RIO kinase 3 acts as a SUFU-dependent positive regulator of Hedgehog signaling. *Cell. Signal.* **25**, 2668–2675 (2013).
78. Q. Xiao *et al*., AMP-activated protein kinase-dependent autophagy mediated the protective effect of sonic hedgehog pathway on oxygen glucose deprivation-induced injury of cardiomyocytes. *Biochem. Biophys. Res. Commun.* **457**, 419–425 (2015).
79. N. Matsumoto *et al*., C3a enhances the formation of intestinal organoids through C3aR1. *Front. Immunol.* **8**, 1046 (2017).
80. Y. Zhang, J. Laterra, M. G. Pomper, Hedgehog pathway inhibitor HhAntag691 is a potent inhibitor of ABCG2/BCRP and ABCB1/Pgp. *Neoplasia* **11**, 96–101 (2009).
81. W. Liu *et al*., Olfactomedin 4 deletion induces colon adenocarcinoma in $Apc^{Min/+}$ mice. *Oncogene* **35**, 5237–5247 (2016).
82. S. Jati *et al*., Wnt5A signaling promotes defense against bacterial pathogens by activating a host autophagy circuit. *Front. Immunol.* **9**, 679 (2018).
83. W. Zhang *et al*.; University of Washington Center for Mendelian Genomics, Expanding the genetic architecture and phenotypic spectrum in the skeletal ciliopathies. *Hum. Mutat.* **39**, 152–166 (2018).
84. K. C. Silveira, C. A. Moreno, D. P. Cavalcanti, Beemer-Langer syndrome is a ciliopathy due to biallelic mutations in IFT122. *Am. J. Med. Genet. A.* **173**, 1186–1189 (2017).
85. T. Mendes Maia, D. Gogendeau, C. Pennetier, C. Janke, R. Basto, Bug22 influences cilium morphology and the post-translational modification of ciliary microtubules. *Biol. Open* **3**, 138–151 (2014).
86. D. Meng, M. Cao, T. Oda, J. Pan, The conserved ciliary protein Bug22 controls planar beating of *Chlamydomonas flagella*. *J. Cell Sci.* **127**, 281–287 (2014).
87. M. Takahara *et al*., C11ORF74 interacts with the IFT-A complex and participates in ciliary BBSome localization. *J. Biochem.* **165**, 257–267 (2019).
88. V. Joukov, A. De Nicolo, A. Rodriguez, J. C. Walter, D. M. Livingston, Centrosomal protein of 192 kDa (Cep192) promotes centrosome-driven spindle assembly by engaging in organelle-specific Aurora A activation. *Proc. Natl. Acad. Sci. U.S.A.* **107**, 21022–21027 (2010).
89. M. A. Gomez-Ferreria, M. Bashkurov, M. Mullin, A.-C. Gingras, L. Pelletier, CEP192 interacts physically and functionally with the K63-deubiquitinase CYLD to promote mitotic spindle assembly. *Cell Cycle* **11**, 3555–3558 (2012).
90. Z.-C. Fan *et al*., *Chlamydomonas* IFT70/CrDYF-1 is a core component of IFT particle complex B and is required for flagellar assembly. *Mol. Biol. Cell* **21**, 2696–2706 (2010).
91. N. Pathak, T. Obara, S. Mangos, Y. Liu, I. A. Drummond, The zebrafish *fleer* gene encodes an essential regulator of cilia tubulin polyglutamylation. *Mol. Biol. Cell* **18**, 4353–4364 (2007).
92. N. Pathak, C. A. Austin, I. A. Drummond, Tubulin tyrosine ligase-like genes *ttll3* and *ttll6* maintain zebrafish cilia structure and motility. *J. Biol. Chem.* **286**, 11685–11695 (2011).
93. N. H. Kelly, N. P. T. Huynh, F. Guilak, Single cell RNA-sequencing reveals cellular heterogeneity and trajectories of lineage specification during murine embryonic limb development. *Matrix Biol.* **89**, 1–10 (2020).
94. K. Howe *et al*., The zebrafish reference genome sequence and its relationship to the human genome. *Nature* **496**, 498–503 (2013).
95. A. M. Session *et al*., Genome evolution in the allotetraploid frog *Xenopus laevis*. *Nature* **538**, 336–343 (2016).
96. S. R. Keenan, C. W. Beck, Xenopus Limb bud morphogenesis. *Dev. Dyn.* **245**, 233–243 (2016).
97. J. Yang, P. Andre, L. Ye, Y.-Z. Yang, The Hedgehog signalling pathway in bone formation. *Int. J. Oral Sci.* **7**, 73–79 (2015).
98. B. Gao *et al*., Mutations in IHH, encoding Indian hedgehog, cause brachydactyly type A-1. *Nat. Genet.* **28**, 386–388 (2001).
99. S. H. Hwang *et al*., The G protein-coupled receptor Gpr161 regulates forelimb formation, limb patterning and skeletal morphogenesis in a primary cilium-dependent manner. *Development* **145**, dev154054 (2018).
100. P. Geetha-Loganathan, S. Nimmagadda, M. Scaal, Wnt signaling in limb organogenesis. *Organogenesis* **4**, 109–115 (2008).
101. P. Kuss *et al*., Regulation of cell polarity in the cartilage growth plate and perichondrium of metacarpal elements by HOXD13 and WNT5A. *Dev. Biol.* **385**, 83–93 (2014).
102. J. Saari, M. A. Lovell, H.-C. Yu, G. A. Bellus, Compound heterozygosity for a frame shift mutation and a likely pathogenic sequence variant in the planar cell polarity—Ciliogenesis gene *WDPCP* in a girl with polysyndactyly, coarctation of the aorta, and tongue hamartomas. *Am. J. Med. Genet. A.* **167A**, 421–427 (2015).

103. T. D. Capellini *et al*., Pbx1/Pbx2 requirement for distal limb patterning is mediated by the hierarchical control of Hox gene spatial distribution and Shh expression. *Development* **133**, 2263–2273 (2006).
104. N. Brison, P. Debeer, P. Tylzanowski, Joining the fingers: A HOXD13 story. *Dev. Dyn.* **243**, 37–48 (2014).
105. H. J. Sim *et al*., Simple method to characterize the ciliary proteome of multiciliated cells. *J. Proteome Res.* **19**, 391–400 (2020).
106. T. J. van Dam, G. Wheway, G. G. Slaats, M. A. Huynen, R. H. Giles; SYSCILIA Study Group, The SYSCILIA gold standard (SCGSv1) of known ciliary components and its applications within a systems biology consortium. *Cilia* **2**, 7 (2013).
107. M. A. El-Brolosy *et al*., Genetic compensation triggered by mutant mRNA degradation. *Nature* **568**, 193–197 (2019).
108. T. E. Sztal, D. Y. R. Stainier, Transcriptional adaptation: A mechanism underlying genetic robustness. *Dev. Camb. Engl.* **147**, dev186452 (2020).
109. I. A. Drummond *et al*., Early development of the zebrafish pronephros and analysis of mutations affecting pronephric function. *Development* **125**, 4655–4667 (1998).
110. M. Taschner, F. Kotsis, P. Braeuer, E. W. Kuehn, E. Lorentzen, Crystal structures of IFT70/52 and IFT52/46 provide insight into intraflagellar transport B core complex assembly. *J. Cell Biol.* **207**, 269–282 (2014).
111. R. Takei, Y. Katoh, K. Nakayama, Robust interaction of IFT70 with IFT52-IFT88 in the IFT-B complex is required for ciliogenesis. *Biol. Open* **7**, bio033241 (2018).
112. G. Ou, O. E. Blacque, J. J. Snow, M. R. Leroux, J. M. Scholey, Functional coordination of intraflagellar transport motors. *Nature* **436**, 583–587 (2005).
113. K. Boldt *et al*.; UK10K Rare Diseases Group, An organelle-specific protein landscape identifies novel diseases and molecular mechanisms. *Nat. Commun.* **7**, 11491 (2016).
114. S.-R. Hong *et al*., Spatiotemporal manipulation of ciliary glutamylation reveals its roles in intraciliary trafficking and Hedgehog signaling. *Nat. Commun.* **9**, 1732 (2018).
115. B. L. Latour *et al*.; University of Washington Center for Mendelian Genomics; Genomics England Research Consortium, Dysfunction of the ciliary ARMC9/TOGARAM1 protein module causes Joubert syndrome. *J. Clin. Invest.* **130**, 4423–4439 (2020).
116. C. Dafinger *et al*., Mutations in KIF7 link Joubert syndrome with Sonic Hedgehog signaling and microtubule dynamics. *J. Clin. Invest.* **121**, 2662–2667 (2011).
117. M. He *et al*., The kinesin-4 protein Kif7 regulates mammalian Hedgehog signalling by organizing the cilium tip compartment. *Nat. Cell Biol.* **16**, 663–672 (2014).
118. L. B. Pedersen *et al*., Chlamydomonas IFT172 is encoded by FLA11, interacts with CrEB1, and regulates IFT at the flagellar tip. *Curr. Biol.* **15**, 262–266 (2005).
119. R. O'Hagan *et al*., Glutamylation regulates transport, specializes function, and sculpts the structure of cilia. *Curr. Biol.* **27**, 3430–3441.e6 (2017).
120. M. Uhlén *et al*., Proteomics. Tissue-based map of the human proteome. *Science* **347**, 1260419 (2015).
121. J. Cao *et al*., The single-cell transcriptional landscape of mammalian organogenesis. *Nature* **566**, 496–502 (2019).
122. Y. Du *et al*., A rare TTC30B variant is identified as a candidate for synpolydactyly in a Chinese pedigree. *Bone* **127**, 503–509 (2019).
123. M. Ma, E. Legué, X. Tian, S. Somlo, K. F. Liem Jr, Cell-autonomous hedgehog signaling is not required for cyst formation in autosomal dominant polycystic kidney disease. *J. Am. Soc. Nephrol.* **30**, 2103–2111 (2019).
124. Y. Benjamini, Y. Hochberg, Controlling the false discovery rate: A practical and powerful approach to multiple testing. *J. R. Stat. Soc. Series B Stat. Methodol.* **57**, 289–300 (1995).
125. M. Getwan, S. Schroda, S. Lienkamp, RNA-Seq data for CRISPR/Cas9-targeting of ift80 and ift172 in Xenopus tropicalis. Sequence Read Archive (SRA). https://www.ncbi.nlm.nih.gov/bioproject/PRJNA670560. Deposited 22 October 2020.
126. A. Hoppmann, P. Schlosser, A. Köttgen, genepi-freiburg/GeneSet. GitHub. https://github.com/genepi-freiburg/GeneSet. Deposited 16 July 2020.